

Article

Design, Analysis and Test of a Hyperbolic Magnetic Field Voice Coil Actuator for Magnetic Levitation Fine Positioning Stage

Yiheng Zhou ¹, Baoquan Kou ^{1,*}, He Zhang ¹, Lu Zhang ¹ and Likun Wang ²

¹ School of Electrical Engineering and Automation, Harbin Institute of Technology, 150001 Harbin, China; sethvoler@163.com (Y.Z.); antonyamanda@163.com (H.Z.), zhanglu24@hit.edu.cn (L.Z.)

² College of Electrical and Electronic Engineering, Harbin University of Science and Technology, 150001 Harbin, China; wlkhello@163.com

* Correspondence: koubqhit@163.com

Received: 13 April 2019; Accepted: 10 May 2019; Published: 14 May 2019



Abstract: The multi-degree-of-freedom high-precision positioning system (MHPS) is one of the key technologies in many advanced industrial applications. In this paper, a novel hyperbolic magnetic field voice coil actuator using a rhombus magnet array (HMF-VCA) for MHPS is proposed. Benefiting from the especially designed rhombus magnet array, the proposed HMF-VCA has the advantage of excellent force uniformity, which makes it suitable for multi-degree-of-freedom high-precision positioning applications. First, the basic structure and operation principles of the HMF-VCA are presented. Second, the six-degree-of-freedom force and torque characteristic of the HMF-VCA is studied by three-dimensional finite element analysis (3-D FEA). Third, the influence of structural parameters on force density and force uniformity is investigated, which is conducive to the design and optimization of the HMF-VCA. Finally, a prototype is constructed, and the comparison between the HMF-VCA and conventional VCAs proves the advantage of the proposed topology.

Keywords: voice coil actuator; multi-degree-of-freedom; magnetic levitation; design and analysis

1. Introduction

The multi-degree-of-freedom high-precision positioning system (MHPS) is one of the key technologies in many advanced industrial applications, such as semiconductor lithography, scanning tunneling microscope, chemistry and biomedical science [1–7]. Generally, the MHPS can be realized by three solutions: stacking linear actuators, planar actuators [1,8,9], and combining coarse positioning stage (CPS) and fine positioning stage (FPS) [10–12]. Benefiting from the two-stage structure, the third solution becomes a widely adopted scheme, which can simultaneously satisfy the requirements of long stroke and high accuracy. Among various FPSs, the magnetic levitation fine positioning stage (MLFPS) is considered to be the state of the art because of its feature of no mechanical contact. In the MLFPS, a stage that integrates multiple actuators and sensors is often adopted, in which the actuator is an electromagnet [13–15], or a voice coil actuator (VCA) [12,16,17]. As a key component of the MLFPS, the performance of actuators strongly determines the MLFPS's positioning ability. Compared with single-degree-of-freedom applications, the MLFPS has special technical requirements for the actuators because of its multi-degree-of-freedom motion. When an actuator works in multi-degree-of-freedom, not only will its output force in the driving direction be influenced by the motion in the other directions, but it will also produce parasitic force and torque, which will reduce the MLFPS's performance and increase the control system's complexity [18]. Therefore, the actuators used in the MLFPS should be designed to be able to output a force which is

independent from the six-degree-of-freedom motion, and in this paper the ability is named as force uniformity. In this paper, we put forward a novel hyperbolic magnetic field voice coil actuator using a rhombus magnet array (HMF-VCA) to achieve this goal, and focus on the analysis of its complex six-degree-of-freedom force and torque characteristics.

2. Basic Structure and Operating Principle

2.1. Basic Structure

Figure 1 shows the structure of the proposed HMF-VCA and MLFPS. The HMF-VCA consists of two components, i.e., stator and mover. The stator consists of two rectangular stator coils with cooling duct, and a non-ferromagnetic stator frame. The mover consists of a rhombus magnet array, a non-ferromagnetic auxiliary frame, and a non-ferromagnetic mover frame. The rhombus magnet array consists of four cubic mover magnets which are arranged on the four edges of a rhombus, and the magnetization is shown as arrows. The MLFPS is made up of a load stage, a fixed base, three vertical HMF-VCA, three horizontal HMF-VCA, three magnetic springs, six relative position sensors, and the corresponding drive and control system. To reduce heat generation and mechanical coupling on the moving part, most devices with cables are installed on a fixed base. It should be noted that the liquid cooling system is optional, depending on the practical application.

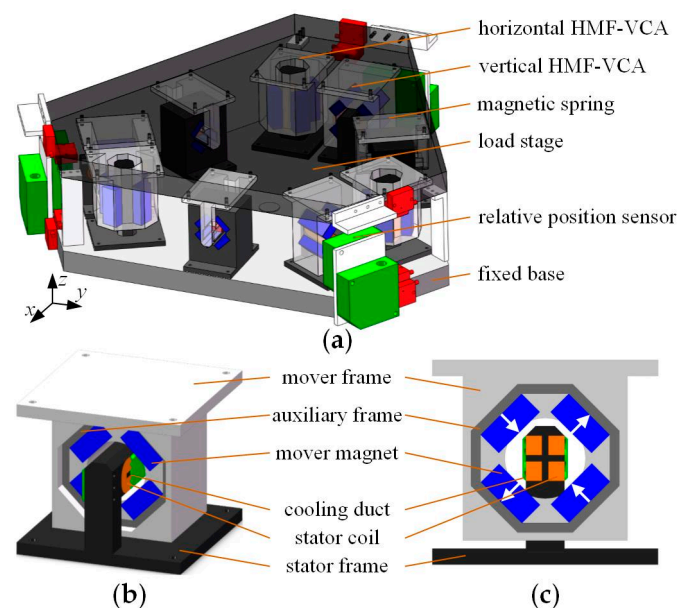


Figure 1. Structure of the HMF-VCA and MLFPS. (a) 3-D view of the MLFPS. (b) 3-D view of the HMF-VCA. (c) Sectional view of the HMF-VCA.

2.2. Operating Principles

Similar to conventional VCAs, the HMF-VCA also works based on the Lorenz force law. The difference between the HMF-VCA and conventional VCAs is their different magnetic field distribution. Figure 2 shows the structure of four types of conventional VCAs which are used in high-precision applications, i.e., VCA with four rectangular magnets (FR-VCA), and VCA with one rectangular or square or circular magnet (OR/OS/OC-VCA) [18], and Figure 3 shows the magnetic field distribution and output force of these VCAs. The magnetic field distribution is calculated with Ansys Maxwell 2D. The materials of permanent magnets and coils are set to be NdFeB35 ($H_c = 890$ kA/m, $B_r = 1.23$ T) and copper, respectively. The current density in the coils is set to be 5 A/mm². The parameters in Figure 3 are set as follows: in Figure 3a, $w_{m1} = 5.4$ mm, $t_{m1} = 2.539$ mm, $w_{c1} = 5.7$ mm, $t_{c1} = 3.6$ mm, $w_{s1} = 2.5$ mm, $w_{s2} = 2.2$ mm, $t_{s1} = 1$ mm, model depth 64.64 mm; in

Figure 3b, $w_{m2} = 9.5$ mm, $t_{m2} = 5.12$ mm, $w_{c2} = 8.9$ mm, $t_{c2} = 6.3$ mm, $w_{s3} = 3.7$ mm, $t_{s2} = 1$ mm, model depth 59.3 mm; in Figure 3c, $w_m = 18$ mm, $t_m = 8$ mm, $w_c = 6$ mm, $t_c = 5$ mm, $w_s = 2$ mm, $t_s = 2$ mm, $y_q = 8$ mm, $z_q = 8$ mm, model depth 36.86 mm. The stroke is set to be ± 0.5 mm \times ± 0.5 mm.

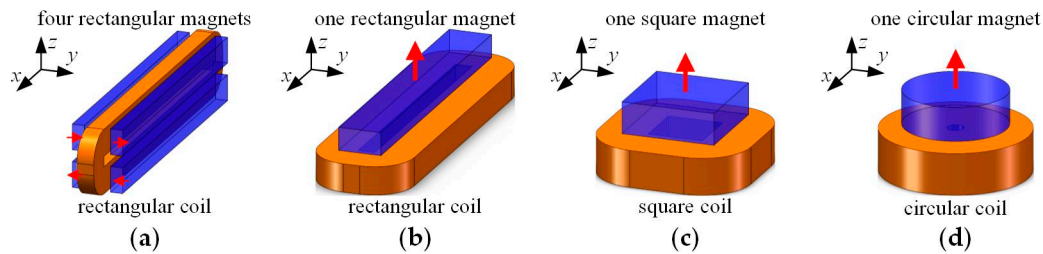


Figure 2. Structure of the conventional VCAs. (a) Structure of the FR-VCA. (b) Structure of the OR-VCA. (c) Structure of the OS-VCA. (d) Structure of the OC-VCA.

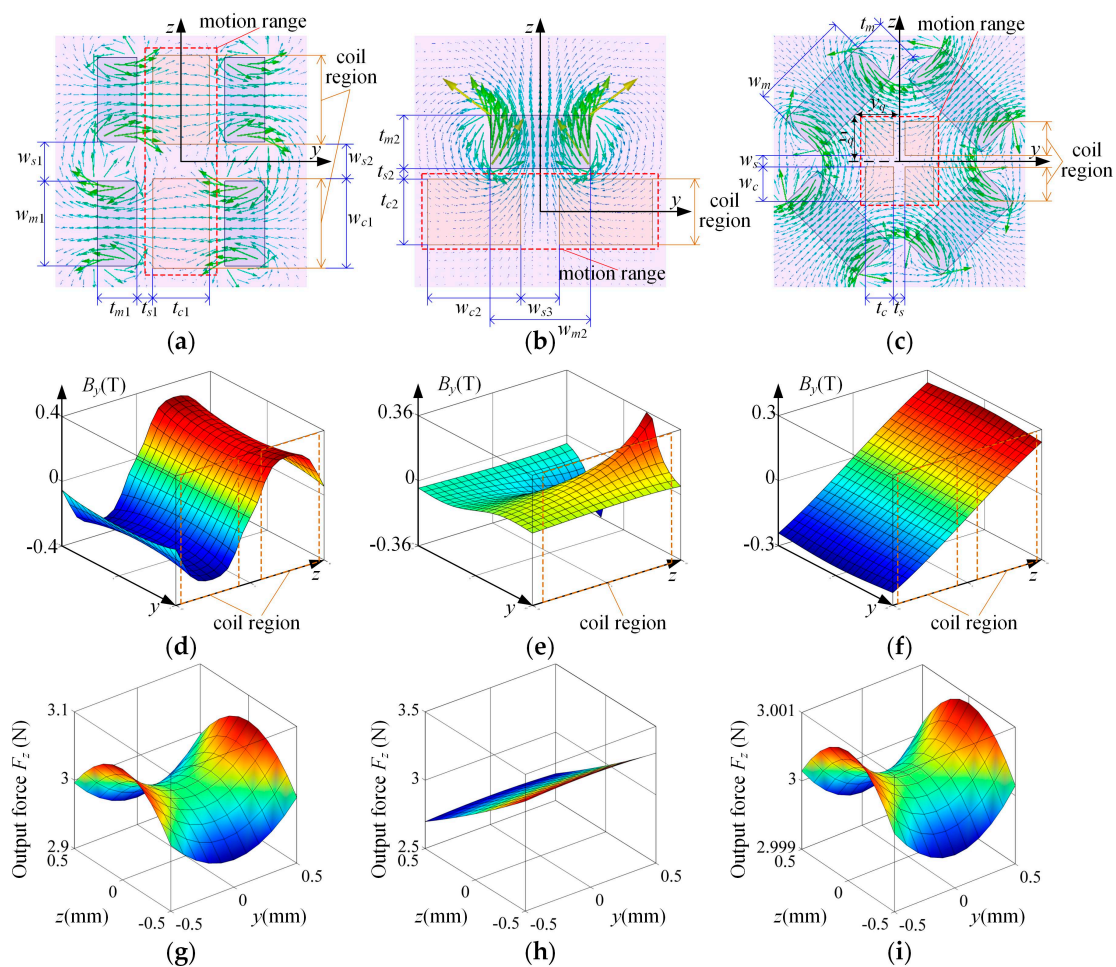


Figure 3. Magnetic field comparison between the HMF-VCA and conventional VCAs. (a) Magnetic field of the FR-VCA. (b) Magnetic field of the OR-VCA. (c) Magnetic field of the HMF-VCA. (d) Magnetic field component B_y of the FR-VCA. (e) Magnetic field component B_y of the OR-VCA. (f) Magnetic field component B_y of the HMF-VCA. (g) Output force F_z of the FR-VCA. (h) Output force F_z of the OR-VCA. (i) Output force F_z of the HMF-VCA.

As shown in Figure 3a,d, the magnetic field in the coil region of FR-VCA is relatively strong, which is beneficial to obtaining higher force density; however, the output force F_z will inevitably change when the coil moves along the z axis, because the magnetic field component B_y is approximately sinusoidal, as shown in Figure 3g.

From Figure 3b,e, it can be seen that the magnetic field component B_y in the coil region of OR-VCA is rather inhomogeneous; although it is occasionally used because of its simple structure, it has the worst force characteristic, as shown in Figure 3h, and this conclusion is also applicable to OS-VCA and OC-VCA.

To obtain better force uniformity, the rhombus magnet array is designed and applied in the HMF-VCA. As shown in Figure 3c, the magnetic field in the HMF-VCA looks like a cluster of hyperbolas. With this hyperbolas-like magnetic field, the magnetic field component B_y is proportional to the value of z , as shown in Figure 3f. In this case, when the mover moves relative to the stator, the increase (decrease) of the force acting on the upper part of the stator coils is equal to the decrease (increase) of the force acting on the lower part of the stator coils, thus the output force will remain constant, as shown in Figure 3i, and the HMF-VCA can achieve excellent force uniformity.

In addition, the MLFPS's load stage will be levitated and positioned with at least six HMF-VCA, but this content is not discussed in this paper. We focus on the analysis of the HMF-VCA's six-degree-of-freedom force and torque characteristics.

3. Characteristics Analysis and Optimization

As discussed in Section 1, the mover of the HMF-VCA will move in six-degrees-of-freedom relative to the stator, i.e., it will translate along the x , y , z axis, and rotate around the x , y , z axis, as shown in Figure 4a. Besides the six-degree-of-freedom motion, the levitated mover is also subjected to six-degree-of-freedom force and torque, i.e., the force F_x , F_y , F_z along the x , y , z axis and the torque T_x , T_y , T_z around the x , y , z axis, as shown in Figure 4b.

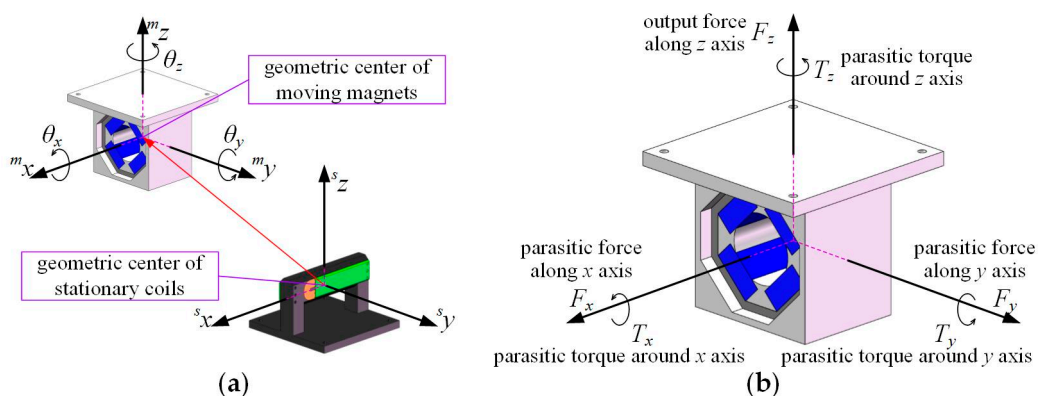


Figure 4. Motion, force and torque of the HMF-VCA. (a) Six-degree-of-freedom motion of the HMF-VCA. (b) The force and torque acting on the mover of the HMF-VCA.

Considering the influence of six-degree-of-freedom motion on the six-degree-of-freedom force and torque, a three-dimensional finite element analysis (3-D FEA) is employed to study the HMF-VCA's complex force and torque characteristic. The analytical method which has the fastest computing speed is another choice to study the characteristic of voice coil actuators, and the related modeling study can be found in [19]. However, there is a modeling error when the analytical method is used to calculate a permanent magnet the permeability of which is not 1 [20]. Therefore, the finite element method is chosen in this paper. The HMF-VCA's structural parameters are listed in Figure 5 and Table 1. The materials of permanent magnets and coils are set to be NdFeB35 ($H_c = 890$ kA/m, $B_r = 1.23$ T) and copper, respectively. The current density in the coils is set to be 5 A/mm². As the two-dimensional magnetic field distribution of the HMF-VCA is given in Figure 3c, it is not repeated here.

According to the analysis of Figure 3c,f, the HMF-VCA's output force will remain constant in its stroke, and the 3-D FEA results shown in Figures 6–11 will prove this.

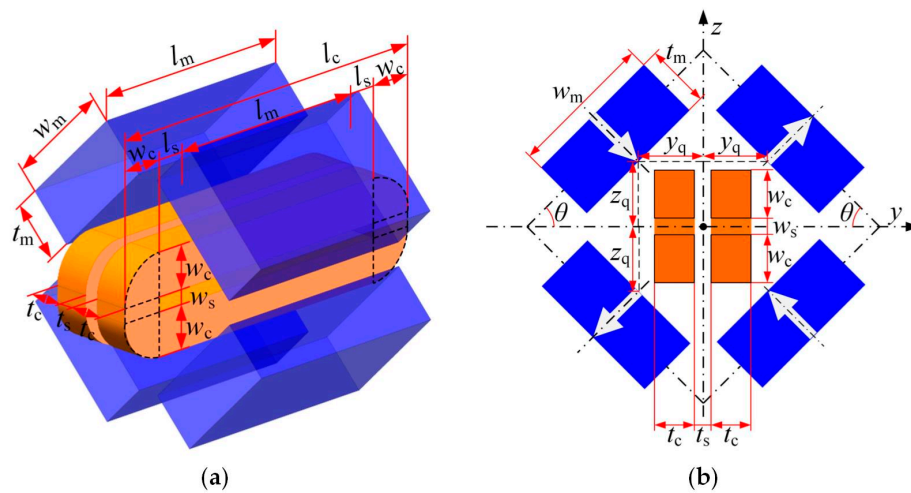


Figure 5. Structural parameters of the HMF-VCA. (a) 3-D view. (b) 2-D view.

Table 1. Structural parameters of the HMF-VCA.

Symbol	Quantity	Data
l_m	length of mover magnet	40 mm
w_m	width of mover magnet	18 mm
t_m	thickness of mover magnet	8 mm
y_q	position of mover magnet in the y axis	8 mm
z_q	position of mover magnet in the z axis	8 mm
θ	inclined angle of mover magnet	45°
l_c	length of stator coil	60 mm
w_c	width of stator coil	6 mm
t_c	thickness of stator coil	5 mm
l_s	adjustable length of stator coil	4 mm
w_s	width of space between stator coils	2 mm
t_s	thickness of space between stator coils	2 mm

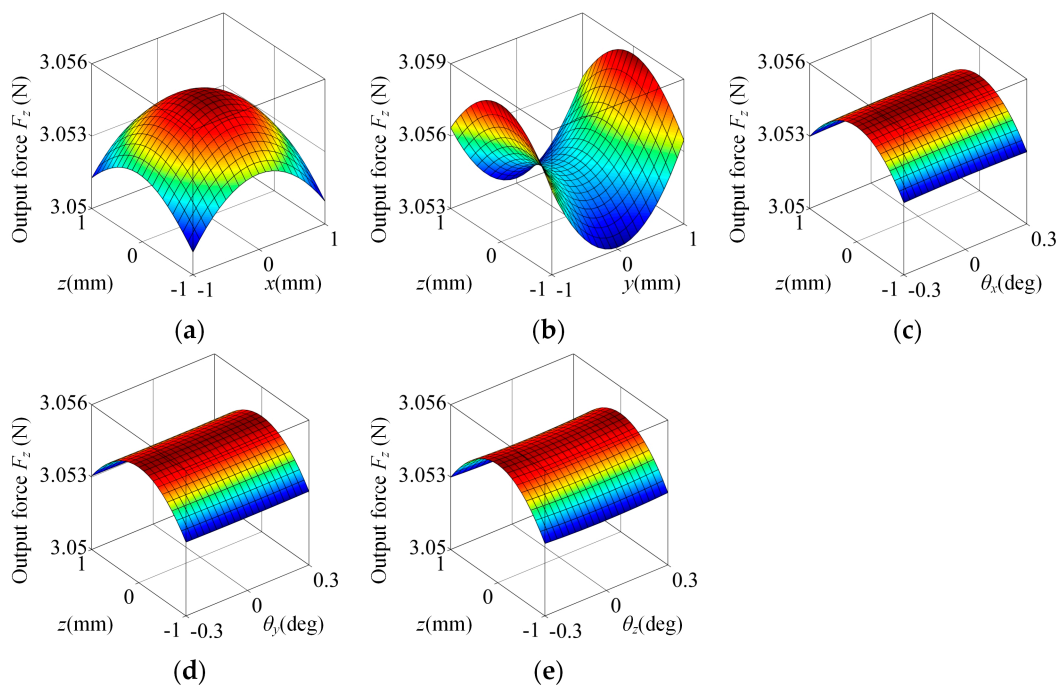


Figure 6. Output force F_z characteristic of the HMF-VCA varied with the mover's motion. (a) F_z vs. z and x . (b) F_z vs. z and y . (c) F_z vs. z and θ_x . (d) F_z vs. z and θ_y . (e) F_z vs. z and θ_z .

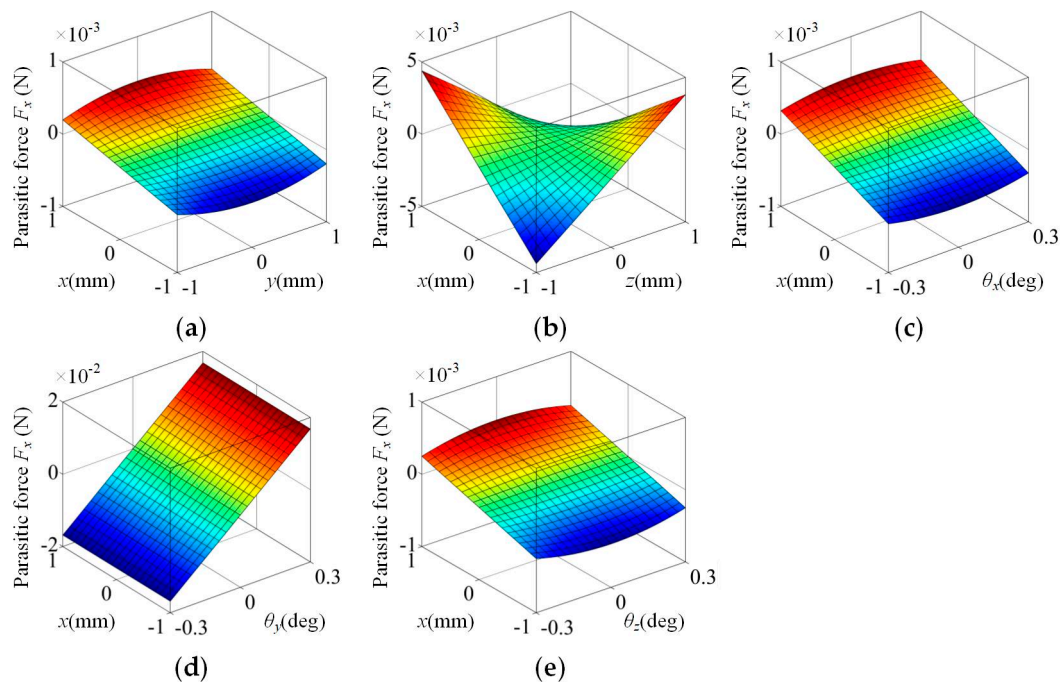


Figure 7. Parasitic force F_x characteristic of the HMF-VCA varied with the mover’s motion. (a) F_x vs. x and y . (b) F_x vs. x and z . (c) F_x vs. x and θ_x . (d) F_x vs. x and θ_y . (e) F_x vs. x and θ_z .

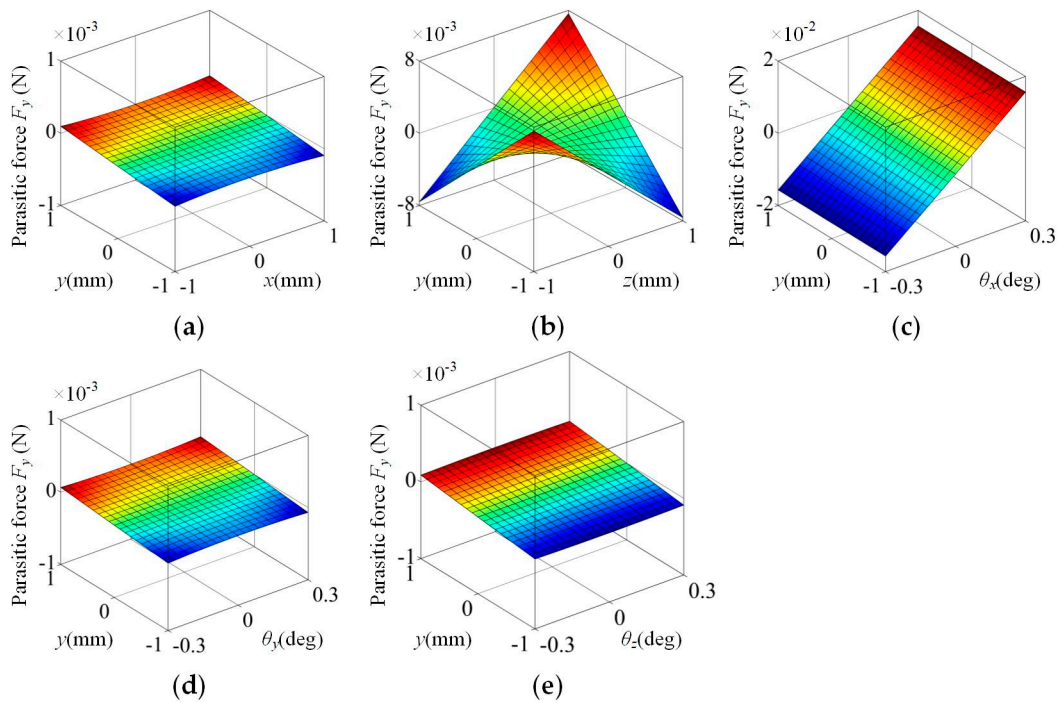


Figure 8. Parasitic force F_y characteristic of the HMF-VCA varied with the mover’s motion. (a) F_y vs. y and x . (b) F_y vs. y and z . (c) F_y vs. y and θ_x . (d) F_y vs. y and θ_y . (e) F_y vs. y and θ_z .

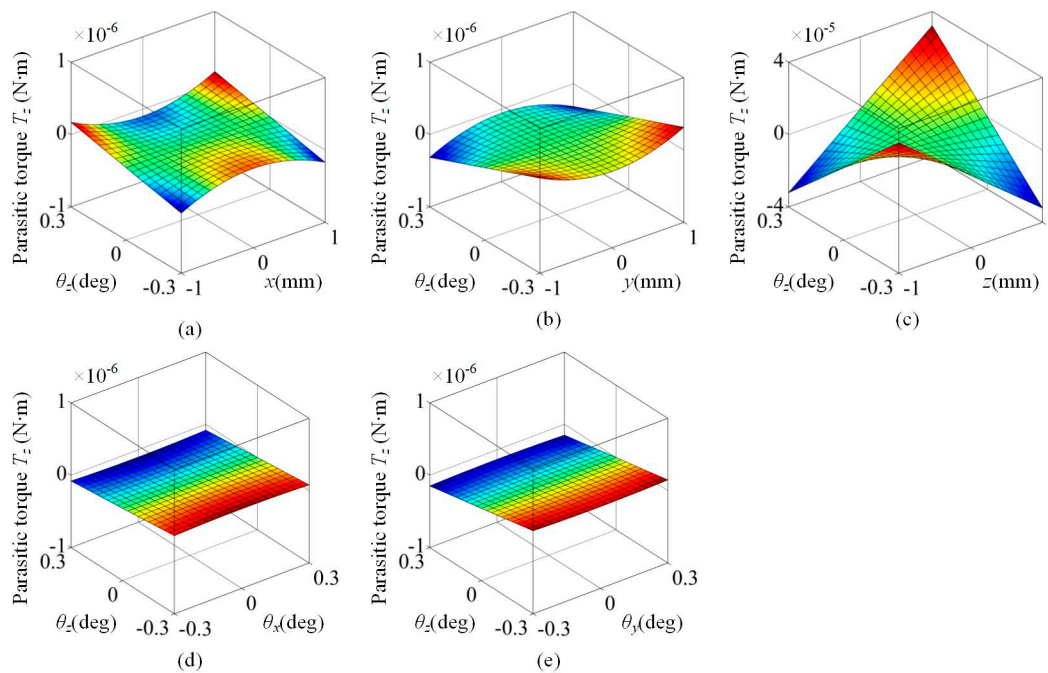


Figure 9. Parasitic torque T_z characteristic of the HMF-VCA varied with the mover's motion. (a) T_z vs. θ_z and x . (b) T_z vs. θ_z and y . (c) T_z vs. θ_z and z . (d) T_z vs. θ_z and θ_x . (e) T_z vs. θ_z and θ_y .

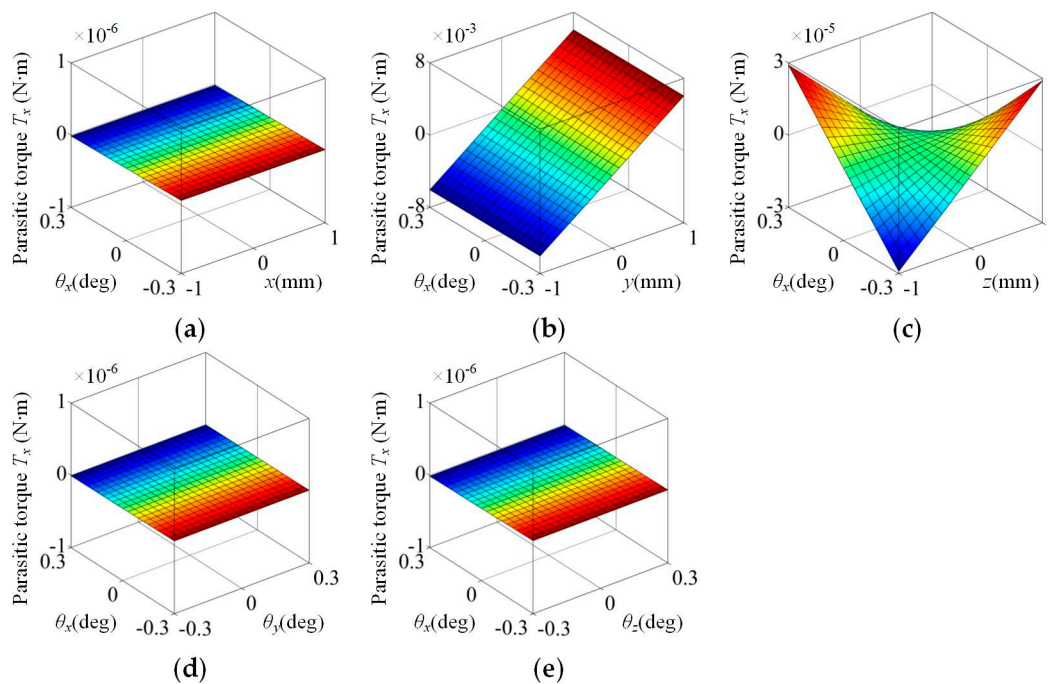


Figure 10. Parasitic torque T_x characteristic of the HMF-VCA varied with the mover's motion. (a) T_x vs. θ_x and x . (b) T_x vs. θ_x and y . (c) T_x vs. θ_x and z . (d) T_x vs. θ_x and θ_y . (e) T_x vs. θ_x and θ_z .

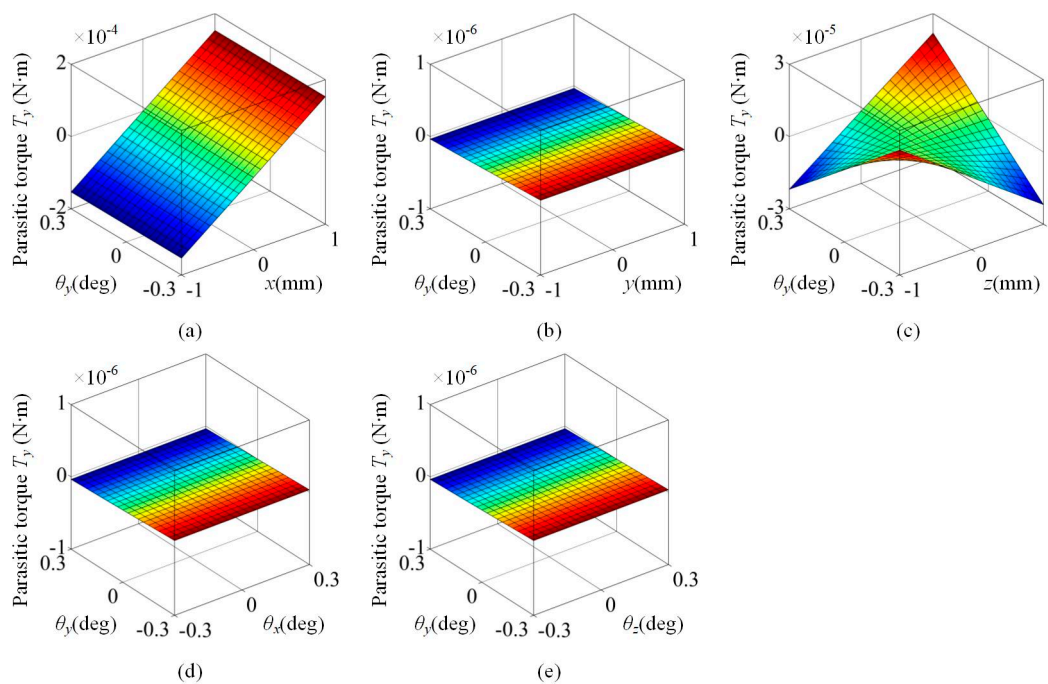


Figure 11. Parasitic torque T_y characteristic of the HMF-VCA varied with the mover's motion. (a) T_y vs. θ_y and x . (b) T_y vs. θ_y and y . (c) T_y vs. θ_y and z . (d) T_y vs. θ_y and θ_x . (e) T_y vs. θ_y and θ_z .

3.1. Output Force

Figure 6 shows the characteristic of the HMF-VCA's output force F_z varied with the mover's motion. From Figure 6, the nominal output force F_z is about 3.055N, and it is almost constant in its full stroke. The variation of F_z caused by the translation or rotation in z , x , y , θ_x , θ_y , θ_z are as small as $0.059\% \text{ mm}^{-1}$, $0.076\% \text{ mm}^{-1}$, $0.121\% \text{ mm}^{-1}$, $0.0044\% \text{ deg}^{-1}$, $0.0022\% \text{ deg}^{-1}$, $0.0092\% \text{ deg}^{-1}$, respectively. This proves that the proposed structure is very effective at reducing the fluctuation of the output force F_z .

3.2. Parasitic Force

Besides the characteristic of the output force F_z , we are also concerned with the characteristics of the parasitic force F_x and F_y , because these two forces are undesirable and would increase the complexity of the control system; thus, these two forces are expected to be as small as possible.

Figures 7 and 8 show the characteristic of the HMF-VCA's parasitic force F_x and F_y varied with the mover's motion. From Figure 7, the parasitic force F_x is approximately proportional to z , θ_y , and it is almost insensitive to the variation of y , θ_x , θ_z . The variations of F_x caused by z , θ_y are $0.143\% \text{ mm}^{-1}$, $1.84\% \text{ deg}^{-1}$, respectively.

Compared with the fluctuation of output force F_z , the fluctuation of parasitic force F_x is much larger. However, we can still say that it has good performance based on the following two reasons. The first reason is that the parasitic force F_x is approximately proportional to z , θ_y . In this case, the adverse effect of parasitic force F_x can be eliminated by adding a compensation coefficient in the control system easily. The second reason is that, in general, the maximum of θ_y in an actual magnetic levitation fine positioning stage (MLFPS) is much smaller than the value set in the simulation. Thus, the parasitic force F_x caused by the rotation around y axis will not be as large as in Figure 7d.

From Figure 8, the parasitic force F_y is approximately proportional to z , θ_x , and it is almost insensitive to the variation of x , θ_y , θ_z . The variation of F_y caused by z , θ_x are $0.250\% \text{ mm}^{-1}$, $1.71\% \text{ deg}^{-1}$, respectively.

Similar to the analysis of parasitic force F_x , although the fluctuation of parasitic force F_y is much larger than the fluctuation of output force F_z , we can still say that it has good performance based on the same two reasons.

3.3. Parasitic Torque

The characteristics of the parasitic torque T_z , T_x and T_y are also taken into account because of their adverse effect on the system, similar to the parasitic force. Figures 9–11 show the characteristic of the HMF-VCA's parasitic torque T_z , T_x and T_y varied with the mover's motion.

Compared with the variation of force, the variation of torque is less obvious. Only when θ_z and z change simultaneously will the parasitic torque T_z change little, as shown in Figure 9, and the parasitic torque T_z is approximately proportional to θ_z , z . Thus, its adverse effect can also be eliminated by adding a compensation coefficient in the control system easily.

At the same time, from Figures 10 and 11, the parasitic torque T_x is approximately proportional to the variation of y , z , θ_x , and the parasitic torque T_y is approximately proportional to the variation of x , z , θ_y . The most significant variations are the variation of T_x caused by y and the variation of T_y caused by x , which are in fact caused by the offset of the output force, and can be solved in the decoupling process of multi-degree-of-freedom system. Thus, they will not increase the control system's complexity. Consequently, the torque characteristic could be ignored in the design and optimization progress.

3.4. Parametric Analysis

Based on the above analysis of Figures 6–11, the HMF-VCA possesses excellent force uniformity as expected. Actually, its performance can be further improved. Several important or relatively large indexes are chosen to be further optimized, i.e., the variation of F_z caused by z , x , y , the variation of F_x caused by z , θ_y , and the variation of F_y caused by z , θ_x . In the following text, these force indexes are abbreviated as $S_{z,z}$, $S_{z,x}$, $S_{z,y}$, $S_{x,z}$, $S_{x,\theta y}$, $S_{y,z}$, $S_{y,\theta x}$, respectively. In addition, considering the volume limitation in some applications, the HMF-VCA's force density (output force per active volume ρ_A) should be also considered and optimized, and it is calculated with the following formula:

$$\rho_A = F_z/V_A = F_z/[4(z_q + w_m \cos \theta + t_m \sin \theta)(y_q + w_m \sin \theta + t_m \cos \theta)(l_m + 2l_s + 2w_c)] \quad (1)$$

where V_A is the active volume of the HMF-VCA, and all the other variables are defined in Figure 5 and Table 1.

To find a useful optimization method for future design, the influence of structural parameters on force density and uniformity are analyzed. For maximum space utilization, there is a geometric relationship for the parameters of coils, $w_c + t_c + 2\delta = y_q + z_q$, and considering the HMF-VCA's stroke and manufacturability, δ , w_s , t_s are chosen to be 3 mm, 2 mm, 2 mm, respectively. Figures 12–14 show the HMF-VCA's force density and uniformity varied with important structural parameters.

Figure 12 shows the HMF-VCA's force density and uniformity varied with y_q and z_q . From Figure 12, the increase of both y_q and z_q will lead to the increase of force density ρ_A ; however, only when y_q and z_q are in particular intervals will the indexes $S_{z,z}$, $S_{z,y}$, $S_{y,z}$ obtain small values. Thus, for the applications where the volume is not limited, y_q and z_q should be set to be the values where $S_{z,z}$, $S_{z,y}$, $S_{y,z}$ obtain small values as shown in Figure 12b,d,g,h, and for the applications where the volume is limited strictly, y_q and z_q should be set to be the values where ρ_A is larger as according to Figure 12a.

Figure 13 shows the HMF-VCA's force density and uniformity varied with w_m and t_m . From Figure 13, it is suggested that a small w_m will be useful for obtaining high force density ρ_A ; however, a larger w_m will lead to better force uniformity. Furthermore, the influence of t_m on force density and uniformity is very small. Thus, similar to the choice of y_q and z_q , w_m should be designed carefully according to the requirements of volume limitation and force uniformity.

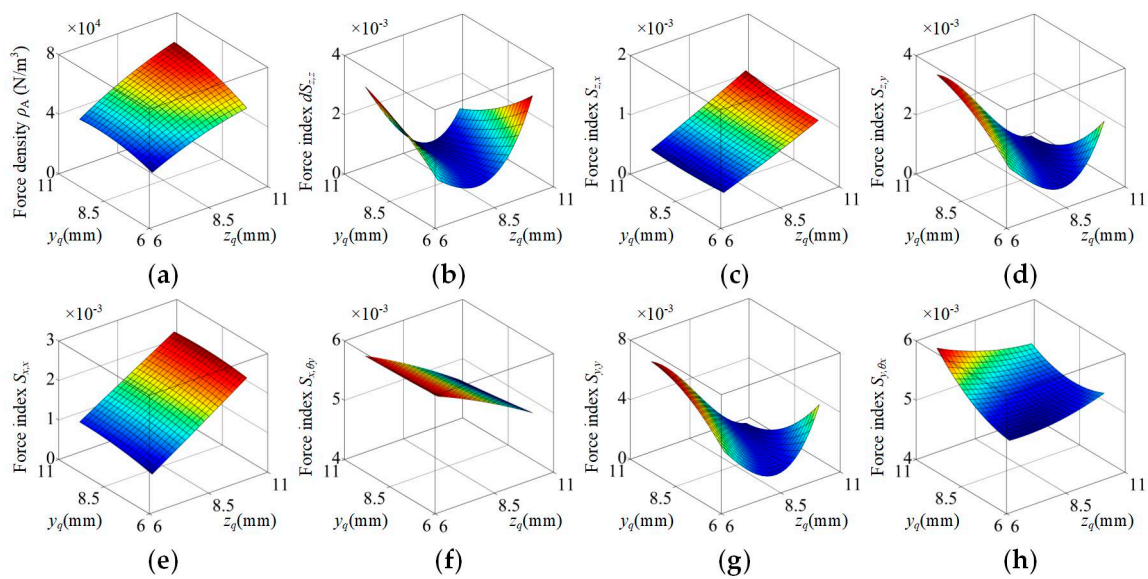


Figure 12. Force density and uniformity of the HMF-VCA varied with structural parameters y_q and z_q . (a) Force density ρ_A . (b) Variation of F_z caused by z . (c) Variation of F_z caused by x . (d) Variation of F_z caused by y . (e) Variation of F_x caused by x . (f) Variation of F_x caused by θ_y . (g) Variation of F_y caused by y . (h) Variation of F_y caused by θ_x .

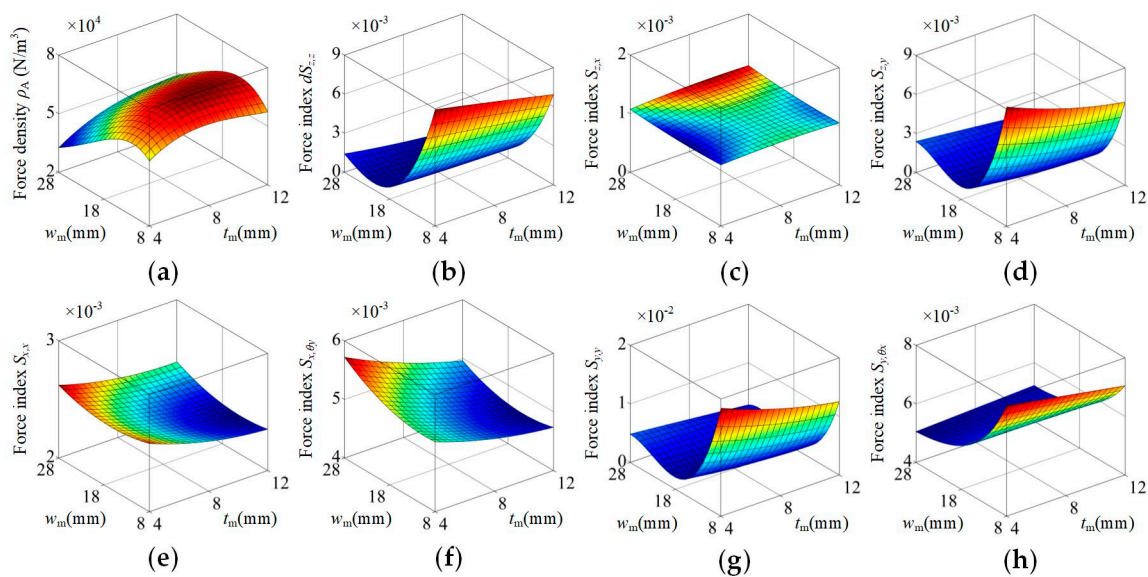


Figure 13. Force density and uniformity of the HMF-VCA varied with structural parameters w_m and t_m . (a) Force density ρ_A . (b) Variation of F_z caused by z . (c) Variation of F_z caused by x . (d) Variation of F_z caused by y . (e) Variation of F_x caused by x . (f) Variation of F_x caused by θ_y . (g) Variation of F_y caused by y . (h) Variation of F_y caused by θ_x .

Figure 14 shows the HMF-VCA's force density and uniformity varied with w_c and l_e . From Figure 14, it is recommended that the parameter w_c be about 6 mm, because the force density and uniformity are improved at the same time. In addition, the increase of parameter l_s can decrease $S_{z,x}$, $S_{x,z}$, but this will also decrease ρ_A and increase $S_{x,\theta y}$.

In conclusion, the change of most of the structural parameters will bring advantages as well as disadvantages, and it is contradictory to reach highest force density and best force uniformity at the same time. Consequently, the researchers should choose reasonable structural parameters according to the actual requirements of force density and uniformity. Further optimization can be achieved

through the multi-parameter optimization method. In this paper, we focus on proving the proposed new topology can achieve good force uniformity, and demonstrating that a topology with good force uniformity can be designed through field analysis and adjusting dimensions. Therefore, the content of multi-parameters optimization is not included in the paper.

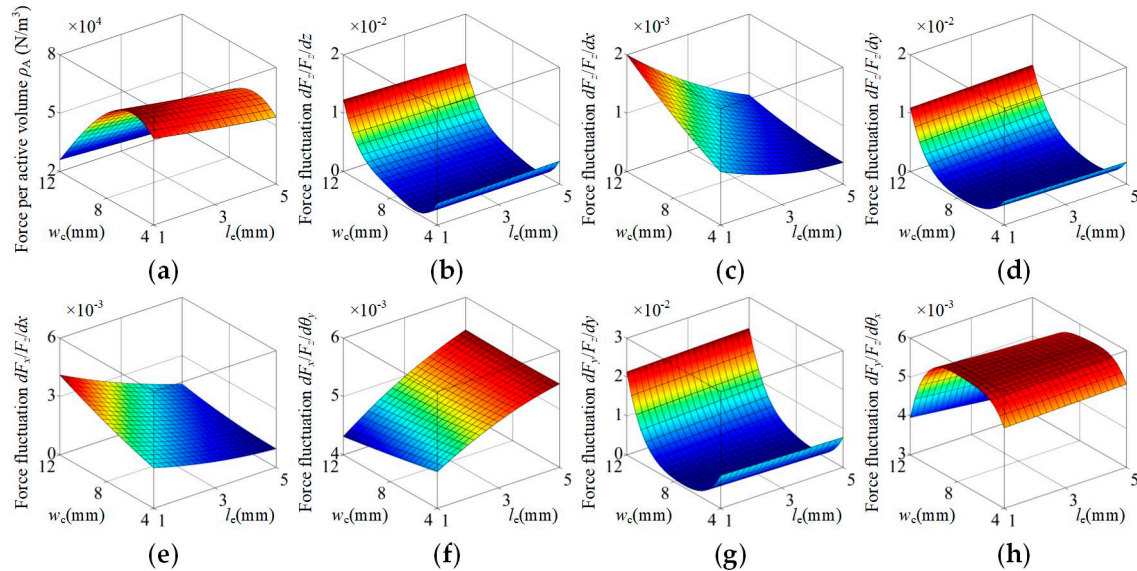


Figure 14. Force density and uniformity of the HMF-VCA varied with structural parameters w_s and l_e . (a) Force density ρ_A . (b) Variation of F_z caused by z . (c) Variation of F_z caused by x . (d) Variation of F_z caused by y . (e) Variation of F_x caused by x . (f) Variation of F_x caused by θ_y . (g) Variation of F_y caused by y . (h) Variation of F_y caused by θ_x .

4. Performance Test and Comparison

A prototype is constructed and tested to validate the performance of the proposed topology. The test installation is made up of a position adjuster, a force sensor, a high-precision multimeter, and a support, as shown in Figure 15a.

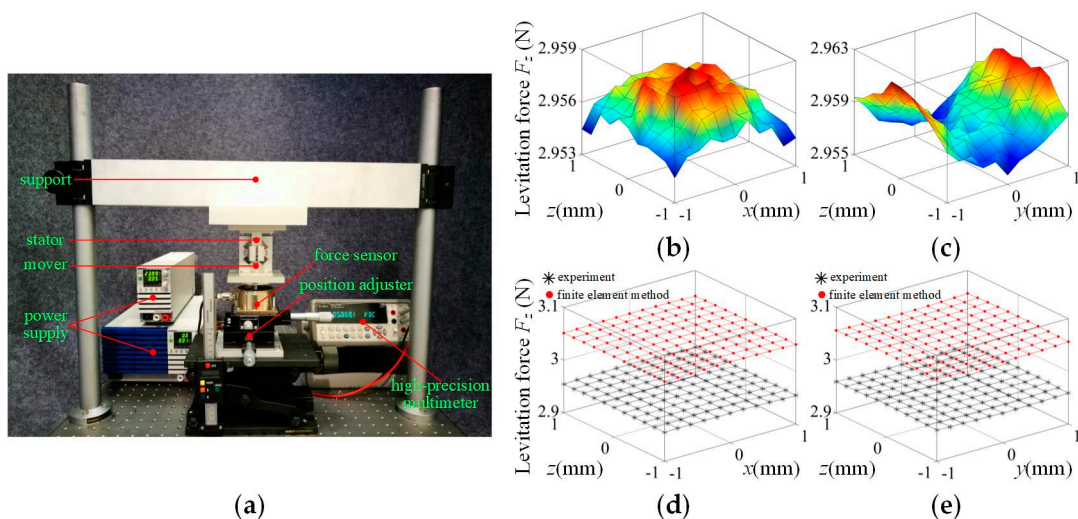


Figure 15. Test installation, and comparison between the test result and FEA result. (a) Test installation. (b) Test result of output force F_z vs. z and x . (c) Test result of output force F_z vs. z and y . (d) Comparison between the test result and FEA result of F_z vs. z and x . (e) Comparison between the test result and FEA result of F_z vs. z and y .

The measured output force is 2.956 N, as shown in Figure 15b. Compared to the FEA value of 3.055 N, the deviation is about 3.24%, and the general trend is in good agreement with the FEA predications. The reasons for the deviation between the measured value and the FEA value are discussed below. The first reason may be that the coils are considered to completely fill the slots in the stator; however, the actual coils are a little smaller than those in the simulation because of the manufacturing process. The second reason may be that the magnets are not perfectly magnetized, in other words, the remanence may be slightly smaller than the simulation value. The third reason may be the deviation of geometric parameters.

5. Discussion

The HMF-VCA is compared with conventional VCAs [18], as listed in Table 2. It should be noted that the stroke of VCAs in [18] is set to be $\pm 5 \times 10^{-4}$ m and $\pm 5 \times 10^{-3}$ rad; thus, the HMF-VCA's performance is also calculated in the same stroke. From Table 2, the HMF-VCA's variation of F_z caused by z , θ_z and variation of F_x caused by x , y are much lower than the other VCAs. Although the HMF-VCA's variation of F_z caused by θ_x or θ_y is larger than the VCAs with one square or circular magnet, the value of 0.001% is small enough for high-precision applications. In addition, the HMF-VCA's variation of F_x and F_y caused by θ_x and θ_y is between the VCA with four rectangular magnets and the VCAs with one square or circular magnet. On the whole, the HMF-VCA features much better force uniformity than conventional VCAs.

Table 2. Performance comparison of VCAs.

Output and Parasitic Force and Torque Characteristic	HMF-VCA	VCA Four Rectangular Magnets	VCA One Rectangular Magnet	VCA One Square Magnet	VCA One Circular Magnet
Variation of F_z caused by z , θ_z	0.018%	1.6%	1.3%	8%	$\approx 8\%$
Variation of F_z caused by θ_x , θ_y	0.001%	0.05%	-	0.0005%	$\approx 0.0005\%$
Variation of F_x caused by x , y	0.006%	-	9%	4%	$\approx 4\%$
Variation of F_x caused by θ_x , θ_y	0.55%	0.17%	-	0.6%	$\approx 0.6\%$
Variation of F_y caused by θ_x , θ_y	0.51%	0.27%	-	4%	$\approx 4\%$

6. Conclusions

In this paper, a novel HMF-VCA has been investigated. Its six-degree-of-freedom force and torque characteristics, as well as the influence of structural parameters on force density and uniformity, are studied by 3-D FEA. The results show that the proposed topology possesses the advantage of excellent force uniformity, and is suitable for MHPS applications.

Author Contributions: Conceptualization, Y.Z.; methodology, Y.Z.; formal analysis, Y.Z.; validation, Y.Z., H.Z., L.Z. and L.W.; investigation, Y.Z.; data curation, Y.Z.; writing—original draft preparation, Y.Z.; writing—review and editing, Y.Z.; project administration, B.K.; funding acquisition, Y.Z., B.K., H.Z., L.Z. and L.W.

Funding: This research was funded by National Natural Science Foundation of China, grant number 51877052, Research and Development Foundation of Scientific and Technological Achievements for Heilongjiang Provincial Universities, grant number TSTAU-C2018002 and CAST-BISEE Foundation, grant number CAST-BISEE2017-007.

Conflicts of Interest: The authors declare no conflict of interest.

References

1. Rovers, J.M.M.; Jansen, J.W.; Compter, J.C.; Lomonova, E.A. Analysis method of the dynamic force and torque distribution in the magnet array of a commutated magnetically levitated planar actuator. *IEEE Trans. Ind. Electron.* **2012**, *59*, 2157–2166. [[CrossRef](#)]
2. Xu, Q. Design and development of a compact flexure-based XY precision positioning system with centimeter range. *IEEE Trans. Ind. Electron.* **2014**, *61*, 893–903. [[CrossRef](#)]

3. Zhang, H.; Kou, B.; Zhang, H.; Jin, Y. A three-degree-of-freedom short-stroke Lorentz-force-driven planar motor using a Halbach permanent-magnet array with unequal thickness. *IEEE Trans. Ind. Electron.* **2015**, *62*, 3640–3650. [[CrossRef](#)]
4. Valiente-Blanco, I.; Diez-Jimenez, E.; Sanchez-Garcia-Casarrubios, J.; Perez-Diaz, J.L. Improving Resolution and Run Outs of a Superconducting Noncontact Device for Precision Positioning. *IEEE-ASME Trans. Mechatron.* **2015**, *20*, 1992–1996. [[CrossRef](#)]
5. Perez-Diaz, J.L.; Valiente-Blanco, I.; Diez-Jimenez, E.; Sanchez-Garcia-Casarrubios, J. Superconducting Non-Contact Device for Precision Positioning in Cryogenic Environments. *IEEE-ASME Trans. Mechatron.* **2014**, *19*, 598–605. [[CrossRef](#)]
6. Devasia, S.; Eleftheriou, E.; Moheimani, S.O.R. A survey of control issues in nanopositioning. *IEEE Trans. Control Syst. Technol.* **2007**, *15*, 802–823. [[CrossRef](#)]
7. Xie, Y.; Tan, Y.; Dong, R. Nonlinear modeling and decoupling control of XY micropositioning stages with piezoelectric actuators. *IEEE-ASME Trans. Mechatron.* **2013**, *18*, 821–832. [[CrossRef](#)]
8. Ueda, Y.; Ohsaki, H. A planar actuator with a small mover traveling over large yaw and translational displacements. *IEEE Trans. Magn.* **2008**, *44*, 609–616. [[CrossRef](#)]
9. Zhu, H.; Teo, T.J.; Pang, C.K. Design and modeling of a six-degree-of-freedom magnetically levitated positioner using square coils and 1-D Halbach arrays. *IEEE Trans. Ind. Electron.* **2017**, *64*, 440–450. [[CrossRef](#)]
10. Jiang, Y.; Zhu, Y.; Yang, K.; Hu, C.; Yu, D. A data-driven iterative decoupling feedforward control strategy with application to an ultraprecision motion stage. *IEEE Trans. Ind. Electron.* **2015**, *62*, 620–627. [[CrossRef](#)]
11. Fung, R.F.; Hsu, Y.L.; Huang, M.S. System identification of a dual-stage XY precision positioning table. *Precis. Eng.* **2009**, *33*, 71–80. [[CrossRef](#)]
12. Choi, Y.M.; Gweon, D.G. A high-precision dual-servo stage using Halbach linear active magnetic bearings. *IEEE-ASME Trans. Mechatron.* **2011**, *16*, 925–931. [[CrossRef](#)]
13. Shan, X.; Kuo, S.K.; Zhang, J.; Menq, C.H. Ultra precision motion control of a multiple degrees of freedom magnetic suspension stage. *IEEE-ASME Trans. Mechatron.* **2002**, *7*, 67–78. [[CrossRef](#)]
14. Chen, M.Y.; Lin, T.B.; Hung, S.K.; Fu, L.C. Design and experiment of a macro–micro planar maglev positioning system. *IEEE Trans. Ind. Electron.* **2012**, *59*, 4128–4139. [[CrossRef](#)]
15. Kuo, S.K.; Meng, C.H. Modeling and control of a six-axis precision motion control stage. *IEEE-ASME Trans. Mechatron.* **2005**, *10*, 50–59. [[CrossRef](#)]
16. Verma, S.; Kim, W.J.; Shakir, H. Multi-axis maglev nanopositioner for precision manufacturing and manipulation applications. *IEEE Trans. Ind. Appl.* **2005**, *41*, 1159–1167. [[CrossRef](#)]
17. Verma, S.; Shakir, H.; Kim, W.J. Novel electromagnetic actuation scheme for multiaxis nanopositioning. *IEEE Tran. Magn.* **2006**, *42*, 2052–2062. [[CrossRef](#)]
18. Vrijsen, N.H.; Jansen, J.W.; Lomonova, E.A. Comparison of linear voice coil and reluctance actuators for high-precision applications. In Proceedings of the 14th International Power Electronics and Motion Control Conference EPE-PEMC 2010, Ohrid, Macedonia, 6–8 September 2010.
19. Zhou, Y.; Kou, B.; Zhang, H.; Luo, J.; Gan, L. Force Characteristic Analysis of a Linear Magnetic Bearing with Rhombus Magnet Array for Magnetic Levitation Positioning System. *IEEE Trans. Magn.* **2017**, *53*, 6500407. [[CrossRef](#)]
20. Kremers, M.F.; Paulides, J.J.; Ilhan, E.; Janssen, J.L.; Lomonova, E.A. Relative Permeability in a 3D Analytical Surface Charge Model of Permanent Magnets. *IEEE Trans. Magn.* **2013**, *49*, 2299–2302. [[CrossRef](#)]

